



The influence of the fiber–matrix microstructure on the energy release rate of off-axis tunnel cracks in laminates

Leon Herrmann ^{a,*}, Lars P. Mikkelsen ^{b,*}, Brian N. Legarth ^c, Christian F. Niordson ^c

^a Chair of Computational Modeling and Simulation, Technical University of Munich, D-80333, Munich, Germany

^b Department of Wind and Energy Systems, Technical University of Denmark, DK-4000, Roskilde, Denmark

^c Department of Civil and Mechanical Engineering, Solid Mechanics, Technical University of Denmark, DK-2800, Kgs. Lyngby, Denmark

ARTICLE INFO

Keywords:

Fracture mechanics
Tunnel cracks
Energy release rate
Microstructure
Laminate
Finite element method
Homogenization

ABSTRACT

Microstructural effects on the energy release rate and the mode mixity for tunneling cracks are investigated. A detailed microstructure is based on scanning electron microscopy of a real laminate. Based on a newly developed two-dimensional off-axis finite element formulation, the dependency of the Mode I, Mode II, and Mode III energy release rates on a range of different layup orientations are investigated. First, the influence of the fiber–matrix microstructures on the energy release rates is assessed and compared to results from homogenized models that exclude explicit representation of the microstructure. A finite element-based homogenization is found to provide consistent and accurate predictions, whereas analytical homogenization methods yield greater discrepancies with respect to a basic stress-based validation case and are thus not recommended in the context of tunneling crack modeling. Secondly, realistic non-straight crack shapes are included in the model resulting in similar energy release rates as for straight cracks in the corresponding fully homogenized models. However, modeling the realistic non-straight cracks without accounting for the specific microstructure provides too low energy release rates when compared to the realistic cases with microstructures.

1. Introduction

Tunnel cracking frequently occurs in layered materials due to differences in ductility and fracture toughness in the layers. Typically, off-axis layers will develop transverse-oriented tunnel cracks (Crossman et al. [1], Tong et al. [2]), impacting adjacent load carrying layers. This is of general importance, but of particular interest when considering fatigue, as these tunnel cracks can act as damage initiation points for both delamination and fiber failure (Raju et al. [3], Jamison et al. [4]). These damage mechanisms have a detrimental impact on the overall stiffness of the laminate with fiber failure leading to an overall collapse of the laminate [5]. Hence, it is of critical importance to gain a quantitative understanding of tunnel cracks, in order to suppress their initiation and propagation, thus enabling improved lifetime predictions of laminated structures.

Several numerical investigations have considered transversely oriented tunnel cracks perpendicular to the main loading direction, by applying two-dimensional plane strain finite element models. In this context, Beuth [6], and Ho and Suo [7] proposed an energy balance method to predict the energy release rate, G , using the crack opening displacement, δ , together with the stress state, σ^0 , of the corresponding

un-cracked case. The stress states were typically estimated by analytical means, whereas the crack opening displacements were estimated numerically using plane strain models.

Studies including detailed fiber–matrix microstructures have been carried out for fibers and cracks oriented at 90° reducing the complexity of the problem and enabling standard plane strain models, such as the study of voids in fiber–matrix microstructures [8], or the study of fiber–matrix debonding using a boundary element method [9,10]. An alternative approach to reduce the complexity of the problem is to assume periodicity of the microstructure, allowing for reduced models based on representative volume elements, such as the study of damage due to voids under plane strain conditions [11], or the estimation of the effective stiffness properties via generalized plane strain models and three-dimensional models for spherical particles [12]. Such models with greatly simplified geometries allows for using sophisticated material models such as isotropic plasticity and even anisotropic plasticity [13,14]. Multiscale models offer yet another alternative, such as in [15], where the problem is analyzed separately at different scales, i.e. the scale of the lamina and the scale of the fiber–matrix interface. An important idealization in the discussed models, as well as the one to

* Corresponding authors.

E-mail addresses: leon.herrmann@tum.de (L. Herrmann), lapm@dtu.dk (L.P. Mikkelsen).

<https://doi.org/10.1016/j.compositesb.2022.110338>

Received 4 August 2022; Received in revised form 26 September 2022; Accepted 30 September 2022

Available online 13 October 2022

1359-8368/© 2022 The Author(s). Published by Elsevier Ltd. This is an open access article under the CC BY license (<http://creativecommons.org/licenses/by/4.0/>).

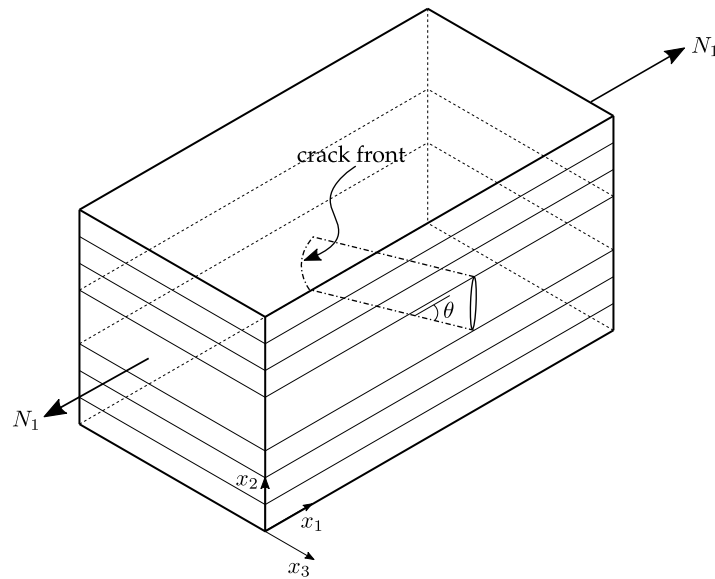


Fig. 1. A laminated structure under a uni-axial load N_1 with an off-axis tunnel crack in the center layer. The crack has an orientation θ w.r.t. the x_1 -axis and the crack growth occurs at the crack front. For further detail of this type of problem, see [16].

be presented in this work is the assumption of a constant cross-section along the fibers, i.e. a perfectly parallel alignment of fibers and cracks.

One major limitation of the models discussed above is their limitation to cracks oriented at 90° , implicit to typical plane strain models, as tunneling cracks can occur at any arbitrary orientation, see Fig. 1 with an indication of the crack front, governed by the lamina layup. This is of particular interest, as tunneling cracks oriented at angles lower than 90° are expected to grow slower due to both greater mixed-mode crack resistance [17] and decreasing energy release rates with smaller tunnel crack angles [16,18]. An accurate analysis of the energy release rate is therefore central in the design phase of a laminate. An orientation different from 90° will lead to a mixed mode crack propagation. Therefore the energy balance method by Ho and Suo [7] was extended by Quaresimin and Carraro [19] and Mikkelsen et al. [16] for orthotropic laminae taking mixed-mode fracture into account, basing crack opening displacements on three-dimensional finite element models with stresses obtained either from classical laminate theory (see e.g. [20]) or three-dimensional finite element models in the context of other defects. These studies were based on the following expression for the steady state energy release rate, G_{ss} , for non-interacting cracks (see [19] for interacting cracks)

$$G_{ss} = G_I + G_{II} = \frac{1}{2h} \int_0^h \sigma_{TT}^0(x_2) \delta_n(x_2) dx_2 + \frac{1}{2h} \int_0^h \sigma_{LT}^0(x_2) \delta_t(x_2) dx_2, \quad (1)$$

where the integration is performed in the global coordinate system (x_1, x_2, x_3) . Here, the layer thickness is h , the laminae stresses (in the absence of a tunnel crack) are denoted by σ_{TT}^0 and σ_{LT}^0 and the normal and tangential crack openings, also referred to as crack face relative opening and sliding displacements in other works, are denoted by δ_n and δ_t , respectively. In the case of non-interacting cracks, the stresses can be computed analytically with classical laminate theory. However, neighboring cracks or microstructures, distort the stress-field, such that it no longer can be constant. This can be taken into account with a numerical simulation of the unopened crack of interest, as shown in [18].

Note also that the stresses are expressed in a local coordinate system $(x_L, x_T, x_{T'})$, where x_T is perpendicular to the crack plane and x_L is aligned with the propagation direction of the tunnel crack. Components defined in the local coordinate system will always be referred to via the subindices L, T, T' , as e.g. the stresses in Eq. (1). A visualization of the local coordinate system with respect to the global coordinate system (x_1, x_2, x_3) is provided in form of a top view of the deformed laminate

in Fig. 2, where the curved lines indicate the tangential variation in the displacement field in the cracked lamina. The global coordinate system employs the subindices 1, 2, 3 and is also illustrated in the 3D sketch in Fig. 1. The global coordinate axis, x_1 , is aligned with the uni-axial load, N_1 , while x_3 is perpendicular to the uni-axial load. For more details on the element formulation including the coordinate systems, see [18]. The same coordinate conventions will be used unaltered throughout this work.

With this formulation, it was possible in [16] to accurately predict the tunneling crack energy release rate using homogeneous three-dimensional finite element models for the computation of the crack opening in terms of δ_n and δ_t . It was, however, infeasible to include the fiber-matrix microstructure in the three-dimensional model, due to the heavy computational cost. However, an important observation made in [16] circumvents the dimensionality issue, as it was observed that the tunneling cracks reach a steady state when far from the boundaries. Thus, the stress and strain fields far ahead and far behind the crack front are invariant in the direction of the crack. This fact enables a projection of the problem to a two-dimensional plane as shown from a top view in Fig. 2, where the tunnel crack is aligned with the fibers indicated in red. This was exploited in [18], where a finite element was proposed, that captures the off-axis behavior with a special two-dimensional kinematic formulation properly accounting for the three-dimensional displacement field. In this kinematic formulation, shown below, the far-field strains $\bar{\epsilon}_{11}, \bar{\gamma}_{12}, \bar{\gamma}_{13}, \bar{\gamma}_{23}, \bar{\epsilon}_{33}$, arising from an imposed far-field loading and treated as additional degrees of freedom, make it possible to define a three-dimensional strain and displacement state in a two-dimensional geometry (see Fig. 3), while accounting for the off-axis orientation $\theta \in]0^\circ, 90^\circ]$. For a detailed explanation on this and derivation, see [18].

$$\begin{aligned} \epsilon_{11} &= u_{1,1} \\ \epsilon_{22} &= u_{2,2} \\ \gamma_{12} &= u_{1,2} + u_{2,1} \\ \gamma_{13} &= \bar{\gamma}_{13} + \cot(\theta) \cdot \bar{\epsilon}_{11} - \cot(\theta) \cdot u_{1,1} + \bar{u}_{3,1} \\ \gamma_{23} &= \bar{\gamma}_{23} + \frac{1}{2} \cot(\theta) \cdot \bar{\gamma}_{12} - \cot(\theta) \cdot u_{2,1} + \bar{u}_{3,2} \\ \epsilon_{33} &= \bar{\epsilon}_{33} - \cot(\theta) \cdot \bar{u}_{3,1} \end{aligned} \quad (2)$$

Combined with the energy balance method this enables efficient and accurate models for the energy release rates for arbitrary laminates and arbitrary tunneling cracks. Due to the efficient two-dimensional framework, investigations can now also be performed for inhomogeneous materials, such as realistic fiber-matrix microstructures.

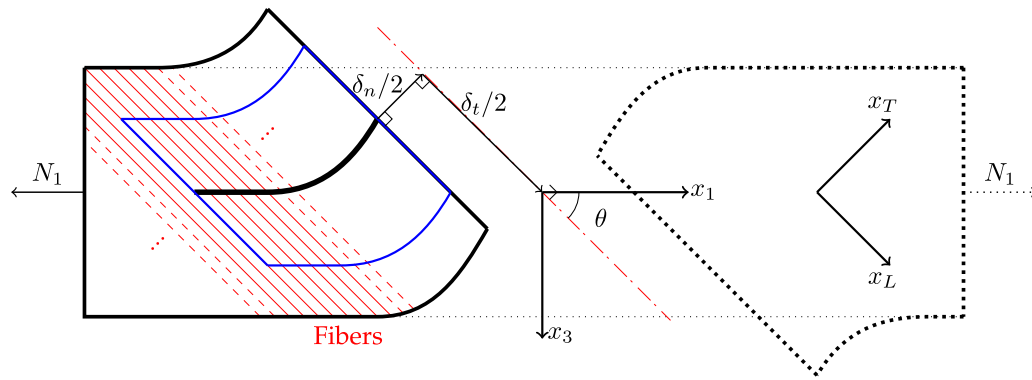


Fig. 2. Deformed symmetry plane showing the laminate from a top-view. The thick bold black line indicates the projection onto the two-dimensional plane. The two-dimensional model is able to accurately represent the behavior inside the blue box far away from the edges. The fibers are indicated in red and are aligned with the tunnel crack direction, x_L . The anti-symmetric curved lines indicates the tangential variation in the displacement field in the cracked lamina. See [18] for more details. (For interpretation of the references to color in this figure legend, the reader is referred to the web version of this article.)

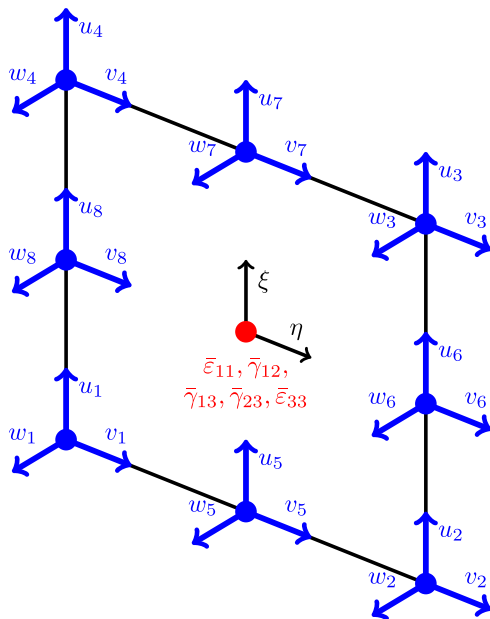


Fig. 3. The off-axis element as a quadratic quadrilateral serendipity element, from [21]. See [18] for more details.

To the best of the authors' knowledge, no work has been conducted on tunneling cracks embedded in fiber–matrix microstructures using either plane strain models or full three-dimensional models, except for a preliminary investigation presented by Carraro et al. [22], that studies the influence of the microstructure on delamination with periodic three-dimensional models.

This paper aims to quantify the accuracy of homogenized material models for the computation of the energy release rate under uni-axial tension when compared to detailed models where realistic microstructures are accounted for. This is accomplished by modeling the microstructure near tunneling cracks in the new special two-dimensional kinematic formulation in [18] and computing the energy release rate by Eq. (1).

2. Problem

2.1. Material system

Inspired by a composite case studied by Mortensen et al. [23], a basalt fiber reinforced epoxy matrix laminate with the symmetric and

balanced layup $[0_4/\theta/0_4/-\theta]_s$ is analyzed under a uni-axial load N_1 applied in the global x_1 -dimension (see Fig. 4). Each layer has the thickness, h , leading to a height of the load-carrying 0° layers of $4h$ and a total laminate thickness of $20h$. The laminate domain extends $2l$ in the x_1 -direction. In [18] a similar layup, $[0/\theta/0/-\theta]_s$, was studied based on homogenized material properties, where symmetry was exploited and only a quarter of the domain was modeled. In this work, a realistic microstructure is considered in the vicinity of the crack, violating the symmetry. Thus a full model including the full domain in all four quadrants has to be considered, see Fig. 4.

The modeled microstructure is indicated by the white domain of length $2L$ in Fig. 4. The crack is aligned with the fiber direction in the central off-axis layer, i.e. at an angle of $-\theta$, see Fig. 2. The discrete fibers are shown by red dots in Fig. 4 as a regular distribution. This particular simple case will be referred to as the *regular case*. In reality, the fiber distribution within a layer is not regular, but rather random (though unidirectional). The lack of regularity invalidate otherwise possible symmetries such that the entire laminate must be modeled, both below and above the x_1 -axis as illustrated by the height $2h$ of the white domain in Fig. 4. Such a distribution based on, for instance, scanning electron microscopy of a real laminate, will be referred to as the *realistic case*. To avoid resolving too many fibers far away from the crack, homogenized orthotropic material properties are adopted outside this domain, whereas the fiber and matrix material inside the microstructure domain are modeled as two distinct isotropic materials: fiber and matrix. Similarly, for the non-cracked layers, a homogenized orthotropic material description is used. In Fig. 4 the domains with homogenized material properties without discrete fiber representation, are shown in gray. Obviously, it is essential, that an appropriate material homogenization method is chosen, which represents the overall mechanical behavior of the microstructural domain accurately.

2.2. Microstructure domain

2.2.1. Realistic case

The distribution of the unidirectional fibers is typically arbitrary with only a few tendencies, as can be seen in microscopy images in e.g. [23] or similar computed tomography images. A realistic fiber distribution is extracted from such an image and will be used for further analysis and, as previously stated, referred to as the *realistic case*. The selected excerpt of such a scan is illustrated in Fig. 5 with a 90° layer between two 0° layers, where the red rectangle highlights the area of interest. Here, the fiber positions and radii, as well as crack shapes, are extracted to create the realistic case shown in Fig. 6. To ease the discretization process, some fiber radii are modified slightly. Several cracks can be identified, from which four crack patterns are selected for the computation of the energy release rate, here denoted as cracks

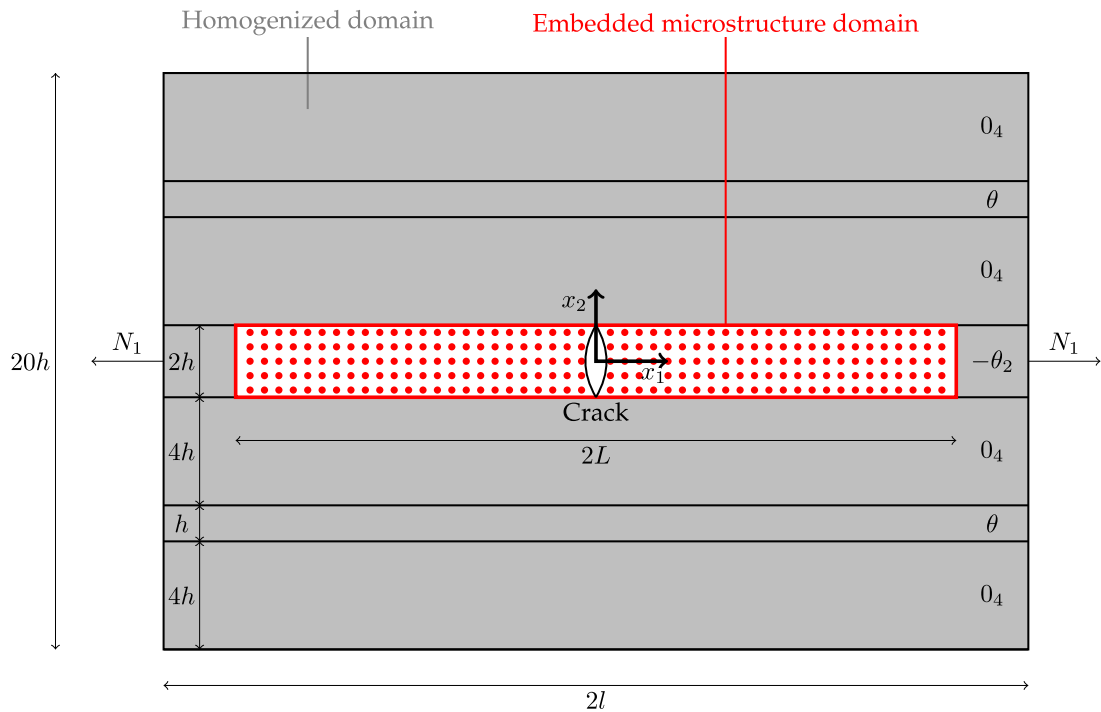


Fig. 4. Laminate model from [18] under a uni-axial load, N_1 , in the global x_1 direction and with two $-\theta$ layers in the center extended to include a discrete microstructure in the proximity of the crack illustrated by the white domain referred to as the embedded microstructure domain. The domain shown in gray is smeared out with a homogenization model.

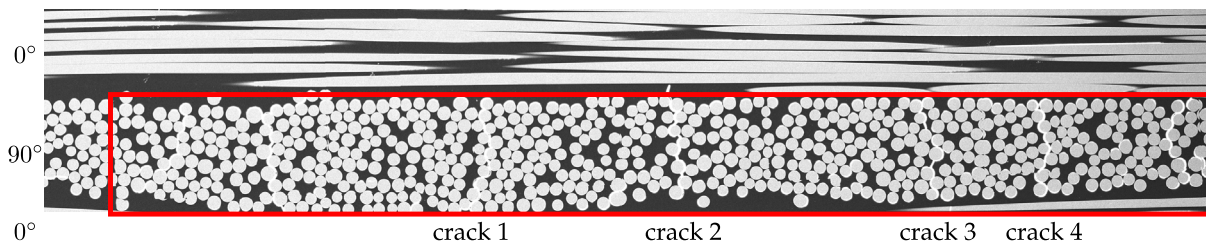


Fig. 5. Scanning electron microscopy image from [23] for the extraction of a realistic fiber distribution and crack patterns.

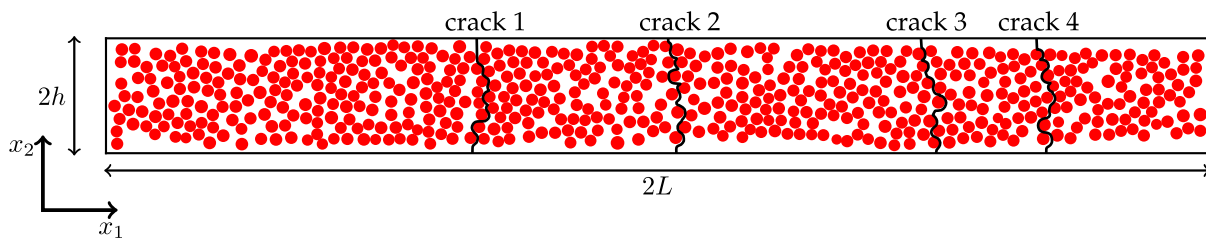


Fig. 6. Extracted realistic case shown with fibers in red and the non-straight tunneling cracks in black, see scan in Fig. 5. (For interpretation of the references to color in this figure legend, the reader is referred to the web version of this article.)

1 to 4 in Figs. 5 and 6. If all four cracks are modeled together, the cracks are interacting. In this work they will first be considered separately, but subsequently two cracks at a time are considered, in which one crack is always assumed to be fully propagated.

2.2.2. Regular case

A second and more simple case, the *regular case*, is also investigated in order to obtain a fundamental understanding of the influence of accounting for a discrete microstructure. In this case, a rectangular array of fibers and a straight crack, as shown in Fig. 7, is investigated. The presented packing was chosen over possibly more realistic structures, such as hexagonal packing, as it allows for straight cracks.

The motivation being to keep the model as simple as possible, while gaining a fundamental understanding of the behavior when including a microstructure. Additionally, it provides a good basis for comparison to the homogenized case with a straight crack. The distances in the modeling plane between the fibers, $2d_1$ and $2d_2$, can be determined from the desired layer height, h , the fiber volume fraction, φ , and the off-axis angle, θ . The layer height, the fiber volume fraction, and the mean fiber radius are chosen identical to the values extracted from the realistic case, Fig. 6. In the regular case, symmetries enable the use of a quarter model as encountered in previous works such as [18,21] (see also red dashed symmetry lines in Fig. 7). Thus, only half the crack height and width are considered.

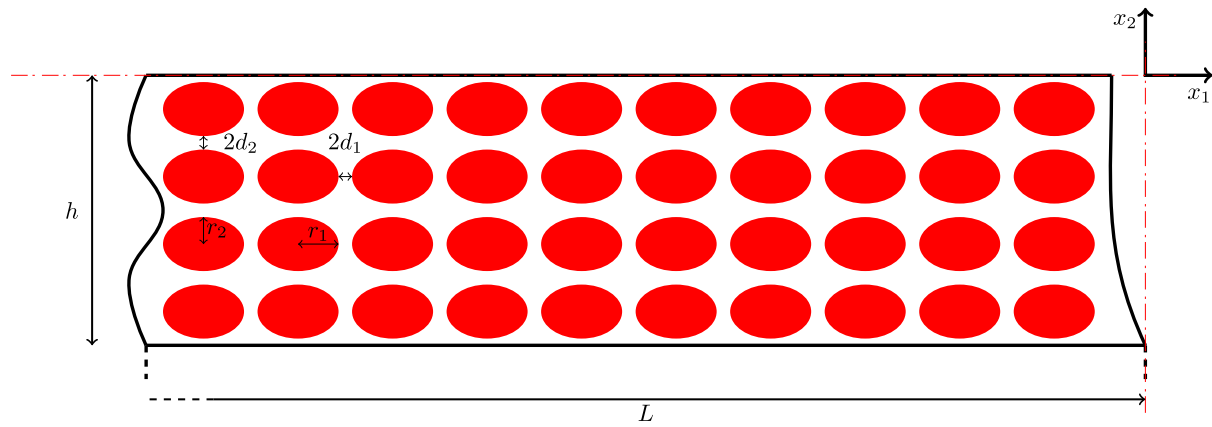


Fig. 7. Regular case.

Table 1
Dimensions of the regular microstructure, see Fig. 7.

φ [-]	r_1 [μm]	r_2 [μm]	d_1 [μm]	d_2 [μm]	Number of fibers through the half height [-]
0.5061	$8.50/\sin(\theta)$	8.50	$2.052/\sin(\theta)$	2.125	4

The model properties are taken directly from the specimen on which the realistic case is based [23]. In [23], the orientation θ was originally 90° , but will be varied in the following analyses to investigate the dependence on the layout angles exploiting the capabilities of the special two-dimensional finite element previously developed [18]. Thus, the geometrical properties r_1 and d_1 are scaled accordingly, see Fig. 7 and Table 1. To get the perpendicular fiber spacings and radii, that are typically used in real measurements, $\theta = 90^\circ$ has to be inserted in the expressions for r_1 and d_1 provided in Table 1. With the change of orientation θ , the distance d_1 and radius r_1 in the modeling plane vary with $1/\sin(\theta)$. The off-axis layer-heights of the laminae (Fig. 4) and the load-carrying layers are $h = 0.085$ mm and $4h = 0.34$ mm, respectively. The fiber radius is nominally given by $r = 8.5$ μm , but as seen in Fig. 5, it varies slightly. All resulting dimensions used for the regular case are listed in Table 1. Note the choice of having a slightly different fiber distances d_1 and d_2 at $\theta = 90^\circ$. The reason for this, was the hard requirement on the layer height h and the volume fraction φ for an appropriate comparison to the realistic case from [23] shown in Fig. 5.

2.3. Homogenized domain

The basalt fiber reinforced epoxy matrix laminate studied by Mortensen et al. [23] have the fiber volume fraction, $\varphi = 0.5061$, and with fiber/matrix properties given in the uppermost rows in Table 2. In the following, it will be assumed that all layers in Fig. 4 have the same fiber volume fraction, φ , and that both the fiber and matrix material are isotropic and exhibit linear elastic behavior. Three different strategies have been investigated in order to estimate the homogenized material properties such that they represent the underlying microstructure as accurately as possible; namely the analytical Voigt–Reuss model, the empirical Halpin–Tsai model, and a finite element based homogenization technique. Detailed descriptions are given in Appendix. The finite element-based approach allows for evaluating both the realistic case (see Fig. 6) and the regular case (see Fig. 7). This distinction is not possible for neither the Voigt–Reuss model nor the Halpin–Tsai model. The finite element analysis leads to two slightly different sets of homogenized properties for the regular and realistic cases. Table 2 shows that the main differences are in the shear moduli, G_{LT} and $G_{LT'}$, and the transverse Poisson's ratio, $\nu_{TT'}$. This effect can be explained by the rectangular packing of the regular microstructure. It can also be observed, that the results from the Halpin–Tsai model are, especially for the transverse stiffnesses, much closer to the finite element results

Table 2
Homogenized material properties for basalt fiber reinforced epoxy, see Mortensen et al. [23]. The fiber and matrix properties are denoted by subscript f and m , respectively, whereas subscripts L, T and T' are homogenized properties. Layer thickness is $h = 0.085$ mm and the mean fiber radius is $r = 8.50$ μm .

φ [-]	E_f [GPa]	ν_f [-]	E_m [GPa]	ν_m [-]
0.5061	85	0.22	3.0	0.40
	Voigt–Reuss	Halpin–Tsai	FEM realistic case (see Fig. 6)	FEM regular case (see Fig. 7)
E_L [GPa]	44.50	44.50	44.04	44.54
E_T [GPa]	5.862	10.53	10.33	11.72
$E_{T'}$ [GPa]	5.862	10.53	10.84	11.81
ν_{LT} [-]	0.3089	0.3089	0.3030	0.3014
$\nu_{LT'}$ [-]	0.3089	0.3089	0.2934	0.3001
$\nu_{TT'}$ [-]	0.4100	0.4100	0.4680	0.4060
G_{LT} [GPa]	2.055	3.833	3.133	3.104
$G_{LT'}$ [GPa]	2.055	3.833	3.529	3.069
$G_{TT'}$ [GPa]	1.071	3.734	3.052	2.302

compared to the properties obtained from the Voigt–Reuss model. Minor differences, up to 1%, e.g. noticeable in the longitudinal Young's modulus E_L , can be explained due to geometrical discretization errors of the circular fibers. Thus, the fiber volume fraction is not fully resolved. The regular case suffers much less from this, as a much finer discretization was possible by using a representative volume with a single fiber.

2.4. Finite element model

The special two-dimensional finite element framework from [18] is used to analyze the problem. The homogenized domain is modeled with 8-noded quadrilateral elements, while the domain of the microstructure is modeled with 6-noded triangular elements due to the challenging geometry. The two elements are fully compatible. The number of degrees of freedom for the regular case varies between 1'000'000 and 2'500'000 depending on the size of the embedded domain, whereas the irregular case was computed with about 15'000'000 degrees of freedom. Computational times range from a few minutes to a few hours, depending on the number of degrees of freedom. An example of the finite element mesh for $\theta = 30^\circ$ is illustrated in Fig. 8, where the contour plot shows the normal strain in the x_1 -direction, ε_{11} .

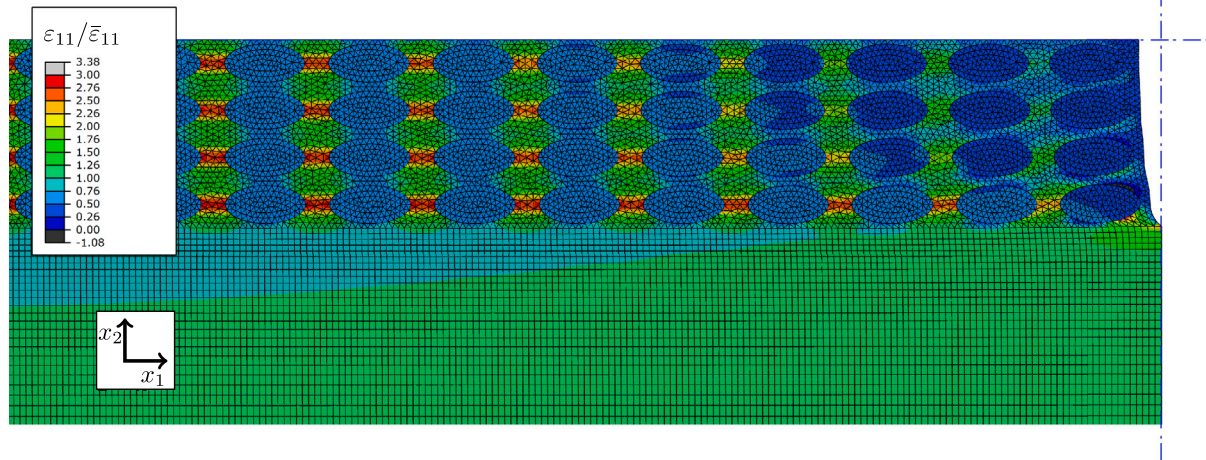


Fig. 8. The mesh used for the microstructure and homogenized domains at $\theta = 30^\circ$. The contour plot shows the normal strain, ϵ_{11} , under an applied uni-axial strain $\bar{\epsilon}_{11}$.

Table 3

Volume-averaged stress components from microstructural finite element simulations compared with classical laminate predictions using three different homogenizing strategies. The results are obtained for $\theta = 30^\circ$ under a uni-axial load corresponding to an applied strain of $\epsilon_{11}^0 = 0.01$ in the x_1 -direction, see also Fig. 8.

	Voigt-Reuss			Halpin-Tsai			FE-based (regular case)		
	σ_{11}	σ_{13}	σ_{33}	σ_{11}	σ_{13}	σ_{33}	σ_{11}	σ_{13}	σ_{33}
Classical Laminate Theory [MPa]	1.78	0.805	0.372	4.04	1.48	0.674	3.90	1.54	0.808
Microstructure with FEM [MPa]	1.87	0.752	0.309	3.93	1.54	0.787	3.93	1.54	0.806
Relative Error [%]	5.2	6.6	17	2.6	4.1	17	0.67	0.16	0.19

2.5. Validation and choice of the homogenization model

The accuracy of the different modeling strategies is validated through a comparison of the stresses in the two domains, i.e. the homogenized (gray) and microstructure (white) domains shown in Fig. 4. This comparison is conducted in the absence of a crack, such that analytical solutions from classical laminate theory (see e.g. [20]) can also be considered. A similar validation approach was used in [18], where the homogenized finite element model was validated against the classical laminate theory. The stresses inside the embedded microstructure domain are of interest as they are needed to evaluate the energy release rate, and they are obtained by a volume average, performed by Gaussian integration over the entire domain of the stress values in the integration points. Subsequently, the stresses are compared to those computed with classical laminate theory using the different homogenization approaches, and a valid homogenized material model should lead to a good agreement. The results for the three homogenization methods are presented in Table 3 for $\theta = 30^\circ$ with the analytical solutions from classical laminate theory as reference values. Similar tendencies were observed for $\theta = 60^\circ$, and $\theta = 90^\circ$, which are not further reported here.

It is observed, that the stresses for the Voigt-Reuss model and the Halpin-Tsai model deviate significantly from the prediction of the classical laminate theory. Errors above 10% are observed for σ_{33} indicating, that these are inaccurate choices for the homogenization approach. However, the homogenized material properties derived from the finite element-based homogenization (with the Abaqus Plugin [24]) applied to the regular case provide a good agreement with errors less than 1%. In addition, as the transverse stiffness of the Voigt-Reuss estimate is significantly lower than the one based on the Halpin-Tsai or the FE-based models, the tangential stresses in this layer, σ_{11} , are also found to be significantly lower (see Table 3).

As only the finite element-based approach results in acceptable errors, the following analyses will only use these material properties, i.e. the two most right columns of Table 2.

2.6. Domain extension for the realistic case

From a modeling perspective, the realistic case distinguishes itself from the regular case through the absence of symmetry. Hence, instead of the quarter model, a full model has to be considered. An example of the deformed crack profile from Fig. 6 (crack 3) at an orientation of $\theta = 30^\circ$ is shown in Fig. 9. It is observed, that the opening of the crack could lead to local sliding contact between crack surfaces normal to the x_2 direction during the crack opening. This is however neglected in the current study. The implication of a contact situation is a higher critical energy release rate, due to the contribution of friction. The impact on the energy release rate would, however, be limited, except in special cases such as friction locking, which is deemed highly unlikely in the encountered situation. The extent of the contact is dependent on the crack shape and the off-axis orientation θ . To take this effect into account a contact formulation is required, which would complicate the comparison with the contactless situation of the regular cases, Fig. 8. Contact on the entire crack surface, i.e. non-locally, may also occur at lower orientations θ , as discussed in [16,21], where an in-depth discussion is provided.

2.7. Evaluation of the energy release rate

The lack of symmetry also introduces shear cracking out of the modeling plane, i.e. Mode III, as the displacements in the x_2 -direction are no longer symmetric. Thereby all three crack modes can be observed. Hence, Eq. (1) has to be extended with the corresponding term for the Mode III energy release rate, G_{III} , computed with the tangential crack opening in the modeling plane, $\delta_{t'}$, aligned with the x_2 -axis, see Fig. 4, and the corresponding stress σ_{LT}^0 , from the uncracked state. The steady-state energy release rate for non-interacting cracks extended

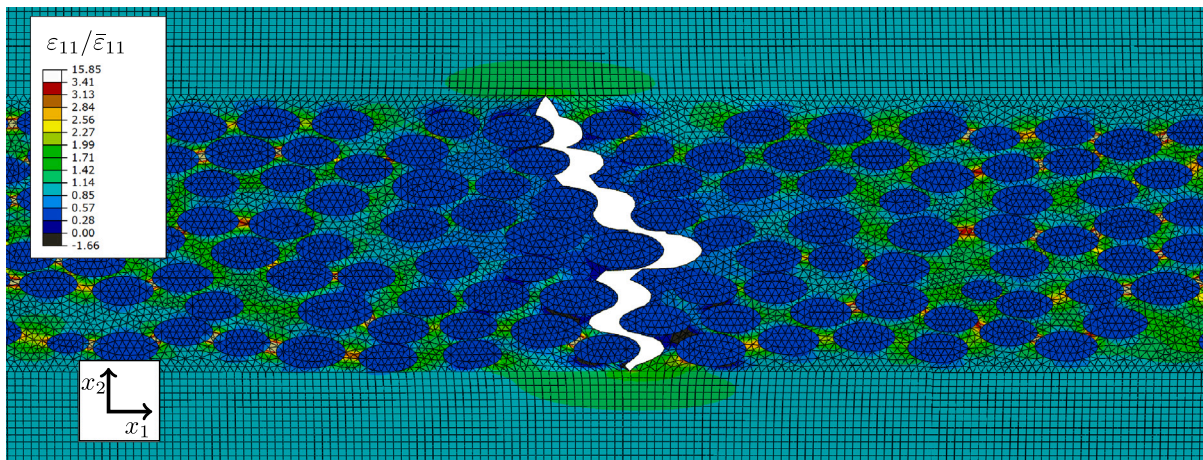


Fig. 9. The crack profile of crack 3 (see Fig. 6) for the realistic case with $\theta = 30^\circ$. The contour plot shows ϵ_{11} under an applied uni-axial strain $\bar{\epsilon}_{11}$. The scaling factor of the displacement is approximately 10.6 at an applied strain of $\bar{\epsilon}_{11} = 0.01$.

from [16] for Mode III is then expressed as

$$\begin{aligned} \mathcal{G}_{ss} &= \mathcal{G}_I + \mathcal{G}_{II} + \mathcal{G}_{III} \\ &= \frac{1}{4h} \int_{-h}^h \sigma_{TT}^0(x_2) \delta_n(x_2) dx_2 + \frac{1}{4h} \int_{-h}^h \sigma_{LT}^0(x_2) \delta_t(x_2) dx_2 \\ &\quad + \frac{1}{4h} \int_{-h}^h \sigma_{LT'}^0(x_2) \delta_{t'}(x_2) dx_2. \end{aligned} \quad (3)$$

Furthermore, the integration is carried out over the entire height from $-h$ to h in global coordinates x_2 , due to the lack of symmetry, also leading to an adjustment in the denominator by a factor of two. The integration performed along the full crack height $2h$ for each energy release rate mode $\mathcal{G}_I, \mathcal{G}_{II}, \mathcal{G}_{III}$, only considers the global crack orientation. Hence a global mode decomposition is used. Details on this choice are provided below. Note also, that the stresses are expressed in local coordinates $x_L, x_T, x_{T'}$, as in Eq. (1).

Due to the arbitrary shape of the crack, it is not trivial to define the mode-mixity. The crack surface is generally not smooth, and mode-mixity varies along the crack front. Furthermore, the normal directions at vertices are not unique and require special treatment. The energy release rate computation via Eq. (3) assumes, that the energy release rate at the crack front, shown in Fig. 1, can be approximated by the stress state far in front of the crack and the crack opening displacement far behind the crack front. For a detailed explanation of this energy balance method, see [6,7]. This implies, that the exact crack tip shape does not have to be considered, which in turn also means, that the variation of mode-mixity along the crack front cannot be determined, which is why a global mode decomposition is employed in Eq. (3). Essentially only the average value of the entire energy release rate is determined rigorously. A pragmatic approach to determining the mode-mixity is based on the evaluation relative to a vertical plane determined by the mean positions of the crack shape. Thus, a distinction is made between the average Mode I energy release rate and the average combined Mode II and Mode III energy release rates. The lack of detailed knowledge of the contributions to the Mode II and Mode III energy release rates is only a concern if there is a great disparity between the fracture resistances with respect to the different modes of fracture. Nevertheless, the average Mode II and Mode III energy release rates are computed separately in the presented approach and shown separately for illustration purposes. These are however only computational quantities and only become physically meaningful when considered in combination.

A further complication arises, due to the increased stress gradients, caused by the abrupt changes in stiffness. In the previous studies [16, 18] as well as for the present regular microstructure cases the energy release rate is computed based on Eq. (1), where small numerical

errors are introduced, due to interpolation errors caused by the stress extrapolation to the nodes. The errors decrease with mesh refinement, which was previously exploited to ensure accurate results. A computationally cheaper alternative is a consistent and equivalent computation to eliminate the interpolation error, where the nodal reaction forces and displacements are used. The change in potential energy $d\Pi$ per unit depth can be expressed via the change in elastic energy per unit depth, which is half of the external work per unit depth according to Clapeyron's theorem [25]. The same approach was also presented in [6],

$$d\Pi = d\Pi_I + d\Pi_{II} + d\Pi_{III} = -\frac{1}{2} \left(\sum_i F_{n_i}^0 \delta_{n_i} + \sum_i F_{t_i}^0 \delta_{t_i} + \sum_i F_{t'_i}^0 \delta_{t'_i} \right), \quad (4)$$

where F^0 are the reaction forces at the crack seam of the uncracked state and δ are the crack opening displacements for the normal direction n , transverse direction t out of the modeling plane, and transverse direction t' in the modeling plane. The change in crack area dA is defined through the effective crack height, l_c , as

$$dA = \frac{l_c}{\sin(\theta)} dx_3, \quad (5)$$

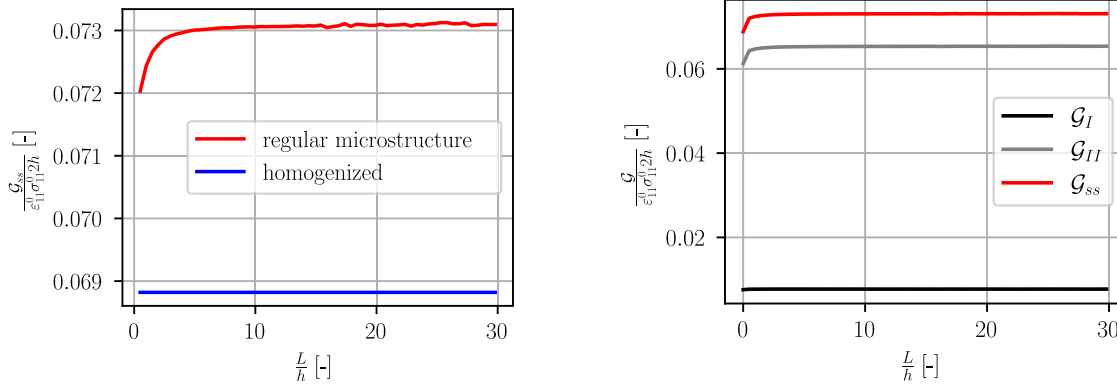
where the increase in crack area due to the off-axis direction is taken into account via the denominator $\sin(\theta)$. Combining Eqs. (4) and (5), the energy release rate, \mathcal{G} , can be computed as

$$\begin{aligned} \mathcal{G} &= \mathcal{G}_I + \mathcal{G}_{II} + \mathcal{G}_{III} = -\frac{d\Pi_I + d\Pi_{II} + d\Pi_{III}}{dA} \\ &= \frac{\sin(\theta)}{2l_c} \left(\sum_i F_{n_i}^0 \delta_{n_i} + \sum_i F_{t_i}^0 \delta_{t_i} + \sum_i F_{t'_i}^0 \delta_{t'_i} \right) dx_3, \end{aligned} \quad (6)$$

where in the case of the straight crack, the effective crack height $l_c = 2h$ is the total height of the cross-section of the tunneling crack in the (x_1, x_2) -plane. By approximating the normal directions of the crack with the macroscopic horizontal crack and using Eq. (6) instead of Eq. (3), the energy release rates of the realistic case may now be evaluated in a more simple manner, while producing the same results.

3. Results

Four investigations have been conducted using the regular case from Fig. 7 and realistic case from Fig. 6. The first three are all inspired by similar studies conducted without the inclusion of a fiber-matrix microstructure in [16,18] and conducted with regular microstructures and straight cracks. First, the influence of the length, L , of the domain with the microstructure is analyzed (see Fig. 4). Secondly, the crack



(a) Comparison of the steady state energy release rates with a homogenized domain and a regular microstructure domain.

(b) Energy release rate modes I and II with the regular microstructure from Fig. 10a.

Fig. 10. Influence of the length of the regular microstructure $\frac{L}{h}$ for $\theta = 30^\circ$, see Fig. 4.

profiles are compared with crack profiles from the corresponding homogenized models without the microstructure. Thirdly, the influence of neighboring cracks in the proximity of the growing tunneling crack is investigated (see also Fig. 6). Finally, non-straight cracks in a realistic microstructure are considered.

3.1. Effect of the size of the embedded regular microstructure domain on the energy release rate

For $\theta = 30^\circ$ Fig. 10 shows the energy release rate for the straight transverse crack, G_{ss} , as well as the corresponding components, G_I and G_{II} for different lengths, $2L$, of the embedded regular microstructure domain, see Fig. 4. The length is normalized by the domain height, $2h$, and the energy release rate is normalized by $\epsilon_{11}^0 \sigma_{11}^0 2h$, as previously in [16,18]. As stated in Table 1 the regular microstructure contains four discrete fibers through the half-height h of the cracked layer (see Fig. 8). In Fig. 10a the energy release rate G_{ss} is shown with and without taking the regular microstructure into account and Fig. 10b provides the components, G_I and G_{II} , together with G_{ss} from Fig. 10a. The homogenized properties obtained from the FEM estimation for the regular case, Table 2, are used.

As expected, if only a small domain is represented by a microstructure, i.e. for $L/h \rightarrow 0$, G_{ss} obtained with a microstructure converges in direction of the result obtained with the homogenized model. However, if the microstructure is taken into account the normalized G_{ss} increases but saturates at a value approximately 6% greater, i.e. from a little below 0.069 to 0.073 (see Fig. 10a). Obviously, no effect of L/h on G_{ss} is seen if the microstructure is excluded ($L/h = 0$), as L/h is a direct measure of the microstructure domain. It is noted that for $\theta = 90^\circ$ the same trend is observed, but with a slightly smaller increase of approximately 5%. If the homogenized properties obtained from the Halpin-Tsai estimation, Table 2, are used instead, the case for $\theta = 30^\circ$ will differ by 17% and 11% for the case of $\theta = 90^\circ$, which further emphasizes that the choice of homogenization model is essential for the accuracy of the results. It is found from Fig. 10a that for $\theta = 30^\circ$ the size of the embedded microstructure domain needs to extend approximately five times the height, i.e. $L/h > 5$, corresponding to the domain length being five times the layer thickness with the tunneling crack. For $\theta = 30^\circ$ an error of less than 1% is obtained for $\frac{L}{h} \gtrsim 1.0$ and for an error less than 0.1% $\frac{L}{h} \gtrsim 6.5$ is required. For $\theta = 90^\circ$ an error of less than 1% is obtained for $\frac{L}{h} \gtrsim 3.5$ whereas an error less than 0.1% can be obtained for $\frac{L}{h} \gtrsim 15.4$. Unless very high accuracy is needed, it is therefore only necessary to model the microstructure in the proximity of the crack in the study of the energy release rate. Fig. 10b shows, that the contribution from G_{II} to G_{ss} dominates over the Mode I contribution in accordance with results presented in [18].

3.2. Effect of the regular microstructure on crack face relative displacements and stress distributions

For $\theta = 30^\circ$, Fig. 11 shows the tunnel crack opening as well as the uncracked stress distribution through the thickness (i.e. along the x_2 -direction). Both results for the case with a regular microstructure (solid line) as well as the case without the microstructure (dashed line) using straight transverse cracks are shown for $L/h = 15.4$. Again, the regular microstructure contains four discrete fibers through the half-height h of the cracked layer (see Fig. 8). These four fibers in the vertical direction are indicated by the four black ellipses illustrating distribution and the cross-section at an angle of $\theta = 30^\circ$. Fig. 11a and b show the normal, δ_n , and the tangential, δ_t , opening of the tunnel crack, respectively. Similarly, Fig. 11c and d show the transverse stress, σ_{TT} , and the shear stress, σ_{LT} , respectively. Especially, for the normal opening in Fig. 11a, very small differences are observed between the two cases. The tangential opening in Fig. 11b shows a slightly larger variation compared to the case without the microstructure. In both cases, the microstructure tends to perturb the crack opening profile in accordance with the presence of the fibers. It is noted, that the tangential opening, δ_t , is approximately three times larger than the normal opening, δ_n . The stress distribution in Fig. 11c and d shows, that the shear stress is larger than the normal stress. As expected, the case without the microstructure shows that both stress components are constant through the thickness of the uncracked layer (dashed line). However, when accounting for the microstructure, both stress components oscillate significantly around the solution without the microstructure, and the peaks of the oscillating solutions coincide with the locations of the stiff fibers.

3.3. Tunnel crack interaction

Fig. 12 shows the energy release rates, G_{ss} , G_I and G_{II} , calculated for different spacing, L_{crack} , between two straight adjacent transverse cracks, for the case of $\theta = 30^\circ$, i.e. three cracks in total. Note that the spacing is normalized by the half thickness of the layer containing the tunnel crack, h , such that an infinite crack spacing corresponds to $h/L_{crack} \rightarrow 0$. Also note, that the first axis is logarithmic as a large span of crack spacings has been evaluated. The steady-state energy release rate, G_{ss} , for the case of a single isolated crack in a regular microstructure from Fig. 10 is included by the blue horizontal dashed line (with value 0.07). As expected, an asymptotic approach to the single crack solution is observed, and for $h/L_{crack} \lesssim 0.1$, the two solutions are almost identical. As for Fig. 10, it is noted, that G_{II} dominates over G_I for the small layup angle of $\theta = 30^\circ$.

The homogeneous case (without microstructure) and the inhomogeneous case (with regular microstructure) exhibit the same tendencies

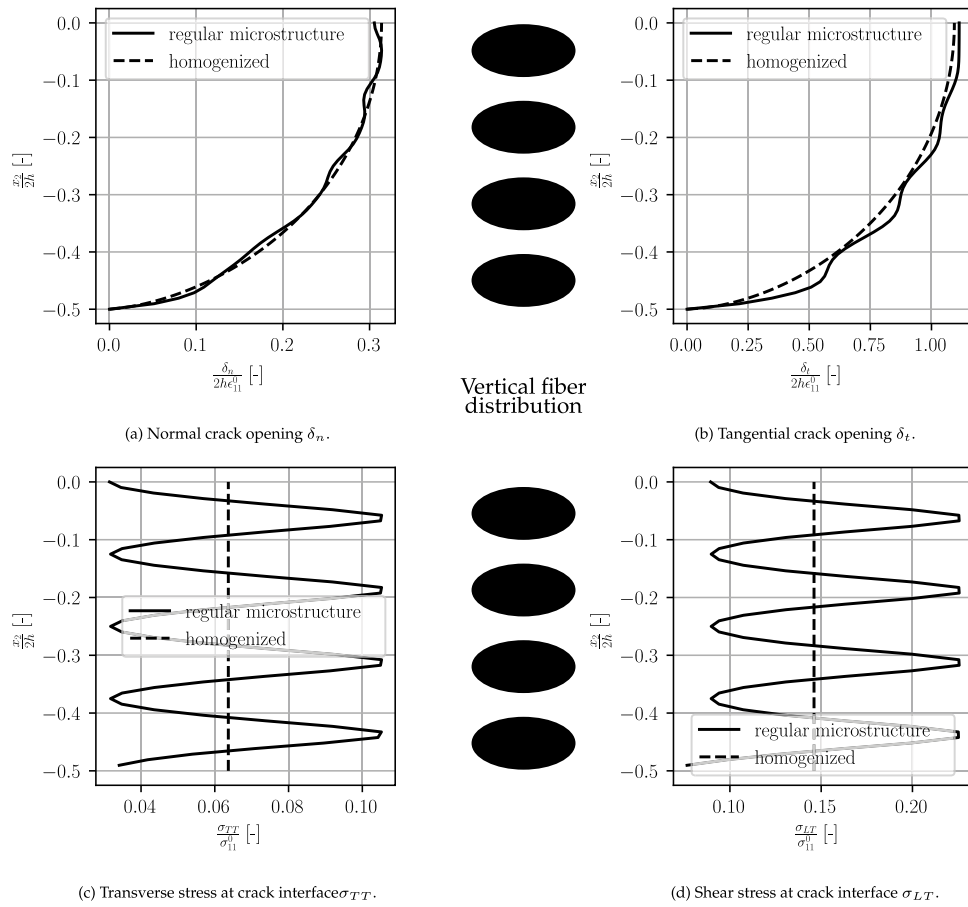


Fig. 11. The crack opening and stress profiles for $\theta = 30^\circ$. (a) and (b) Crack opening displacements. (c) and (d) Stress distributions.

with only minor differences, as can be seen by comparing curves with cross-marks to curves with dot-marks in Fig. 12. If the energy release rate close to zero is neglected, the largest relative error between the cases with or without the microstructure is 5.6%. It can thus be observed, that the influence of nearby cracks is much more important than accounting for an accurate microstructure. Hence, the macroscopic features seem to dominate over the microscopic features in terms of the fiber–matrix microstructure.

3.4. Realistic case

For the realistic case of fiber distribution in Figs. 5 or 6, the homogenized constitutive parameters employed for the layers without microstructure were estimated via finite element-based homogenization based on the microstructure shown in Fig. 6. The properties are provided in Table 2. The length of the embedded fiber–matrix microstructure domain presented in Fig. 4, is approximately $L = 9.8h$, while the length extending the model beyond the embedded model is about $l = 5L = 49h$, which is determined to be sufficiently large through a convergence study monitoring the displacements, the stresses and the energy release rates.

In a first study, all four cracks presented in Fig. 6 are considered individually. Essentially, this reflects four different realistic cases of microstructure allowing an introduction of some statistical assessment. Averaging the results can alleviate the effect of idealizing the fibers and tunnel cracks as being perfectly parallel. Computations were conducted for the orientations $\theta = 30^\circ$, $\theta = 60^\circ$, and $\theta = 90^\circ$ for each crack. For the sake of comparison, three cases are presented with increasing complexity; one treats a homogenized material with a straight crack, a second investigates a homogenized material with a non-straight crack taken from Fig. 5, and finally, the fiber–matrix microstructure is analyzed

Table 4

The energy release rate values behind the data shown in Fig. 13a.

$\theta = 30^\circ$		$\frac{G_I}{\bar{\sigma}_{11}\epsilon_{11}2h_c}$	$\frac{G_{II}}{\bar{\sigma}_{11}\epsilon_{11}2h}$	$\frac{G_{III}}{\bar{\sigma}_{11}\epsilon_{11}2h}$	$\frac{G_{ss}}{\bar{\sigma}_{11}\epsilon_{11}2h}$
Straight crack	All cracks	0.0063	0.075	0	0.081
Non-straight crack	crack 1	0.0052	0.061	0	0.066
	crack 2	0.0048	0.058	0	0.063
	crack 3	0.0049	0.058	0	0.063
	crack 4	0.0047	0.057	0	0.061
Non-straight crack with realistic microstructure	crack 1	0.0060	0.082	0.00027	0.088
	crack 2	0.0057	0.075	0.00012	0.081
	crack 3	0.0056	0.075	0.00019	0.080
	crack 4	0.0056	0.085	0.00024	0.091

with the non-straight crack also from Fig. 5. The results are summarized by bar-plots in Fig. 13 showing the mean of the computed energy release rates of each crack. Additionally, the standard deviations are indicated and it is noted, that only small variations are seen. Individual modeling results are shown in Table 4 for $\theta = 30^\circ$, where it can be seen, that the small Mode III contribution only occurs for the case with a microstructure.

The first important conclusion can be drawn, by reconsidering the results of the regular case as e.g. in Fig. 10, where a convergence of the normalized energy release rate towards $G_{ss} = 0.073$ is observed for $\theta = 30^\circ$. In contrast, the non-straight crack with the homogenization based on the realistic case yields an energy release rate of $G_{ss} = 0.085$, as seen in Fig. 13, leading to a discrepancy of approximately 10%. Therefore, the idealization of the realistic case by using the regular case is deemed insufficient.

Yet another important conclusion can be drawn when solely considering the bar-plots in Fig. 13, where the straight crack without the

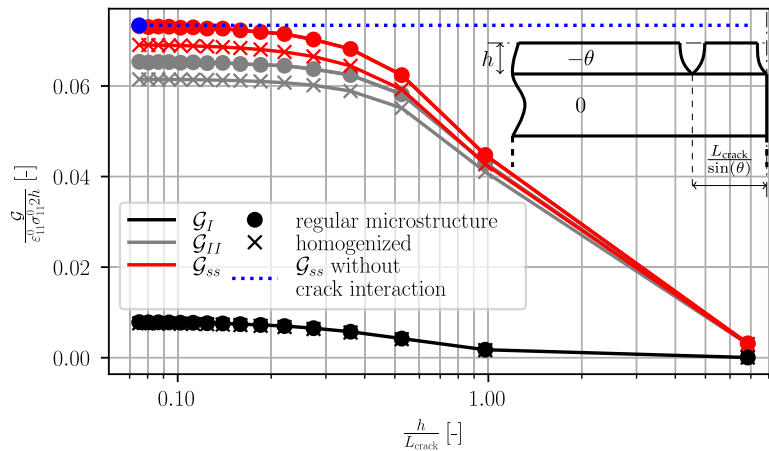


Fig. 12. Influence of the crack spacing $\frac{h}{L_{crack}}$ considering three cracks for $\theta = 30^\circ$ exploiting symmetry. Note that the value at an infinite spacing (horizontal blue dashed line) is reused from Fig. 10 which was computed with the regular microstructure to be 0.07.

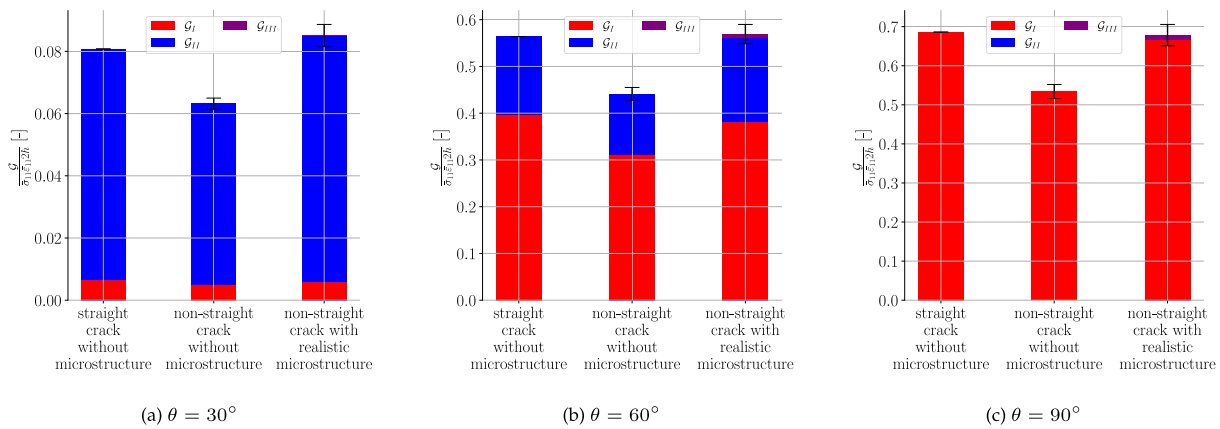


Fig. 13. Energy release rate of straight and non-straight crack in both homogenized and the realistic fiber-matrix microstructure in Fig. 6 for the three orientations $\theta = 30^\circ$, $\theta = 60^\circ$, and $\theta = 90^\circ$.

microstructure (most left bar) and non-straight crack with microstructure (most right bar) yield similar results for all three orientations considered. On the other hand, the cases of non-straight cracks without microstructure (bar in middle) show significantly reduced energy release rates. In other words, the realistic case of a non-straight crack with a microstructure (most right bar) results in a much higher energy release rate than that of the corresponding “realistic” non-straight crack without a microstructure (bar in middle). Hence, it is suggested simply to replace the complex case of the non-straight crack with the microstructure by a straight crack without the microstructure. In an attempt to explain this, the crack profile is investigated in detail. Specifically, crack 3 in Fig. 6 is considered at an orientation of $\theta = 30^\circ$, and the two crack face relative displacements, u , and the crack opening, δ , are illustrated in Fig. 14a and b, respectively. Interestingly, the differences in crack openings are relatively small and not sufficient to explain the differences in the energy release rates. In fact, the non-straight crack cases have greater crack openings, suggesting larger energy release rates. In the absence of a microstructure and in the absence of a crack, the models are identical and thus the stress states as well. Due to the lack of disparity in the crack opening profiles, a similar change in potential energy $d\Pi$ should be expected. Thus, the main factor giving rise to the decrease in the energy release rate seen in Fig. 13 is the change in the crack surface area due to crack growth, see Eq. (6), where a larger effective crack height, l_c , yields a smaller energy release rate. For the cracks 1, 2, 3 and 4, the normalized crack height in the (x_1, x_2) -plane, $l_c/(2h)$, can be found from Fig. 6 to be 1.25, 1.33, 1.32

and 1.37, respectively. The average value is 1.32, which for the non-straight crack suggests a value of about $1/1.32$ or 76% of the energy release rate for the corresponding straight crack. In fact a value of 78% is found from the results presented in Fig. 13, and the discrepancy may thus be explained by the increased crack area together with a slight increase in the crack opening profiles. Note, that in the presence of a microstructure and a non-straight crack the nodal reaction forces, and consequently the stresses, are not identical to the nodal reaction forces and stresses without a microstructure. In the presence of the microstructure, the stresses are larger than without a microstructure. This leads to a similar energy release rate as for the straight crack without a microstructure, despite a similar crack face relative opening and a difference in the crack surface area.

To support the conclusion, that the length of the crack is the most important factor for determining the change in the energy release rate, an additional idealized study is conducted with angled cracks, which would not occur in reality, as straight cracks yield the highest energy release rate. As illustrated in red in Fig. 15(a), the angled crack is considered in the middle layer of the layup $[0_4/\theta/0_4/-\theta]_s$, i.e. the two $-\theta$ -layers. The material in the layers is based on the homogenized properties of the realistic case found in Table 2. The crack is defined by the dimensionless inclination parameter a . Hence, the effective crack height in the (x_1, x_2) -plane can be computed as

$$l_c(a) = 2h\sqrt{1 + \frac{a^2}{4}} \tag{7}$$

If the change of the energy release rate caused by the variation in the crack opening is neglected, the energy release rate at an arbitrary

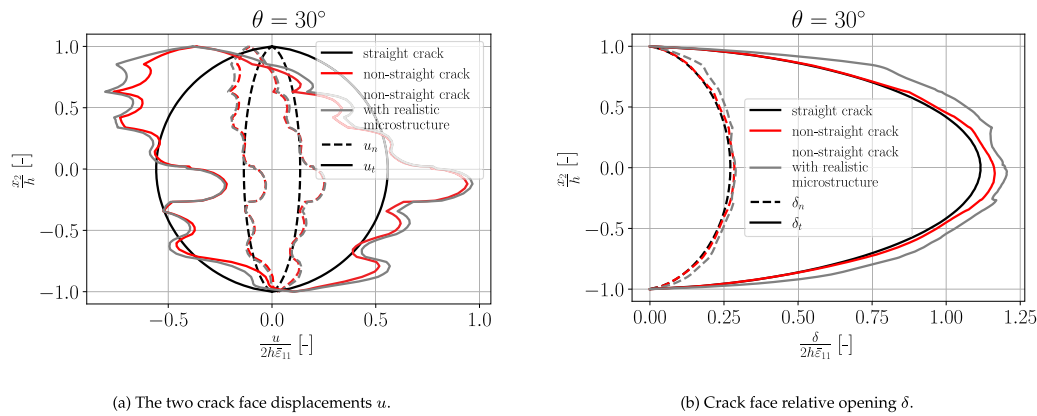


Fig. 14. Comparison of straight and non-straight crack profiles through the height with $\theta = 30^\circ$. The non-straight crack embedded in a realistic fiber–matrix microstructure is crack 3 in Fig. 6, whereas the straight crack is in a homogenized material.

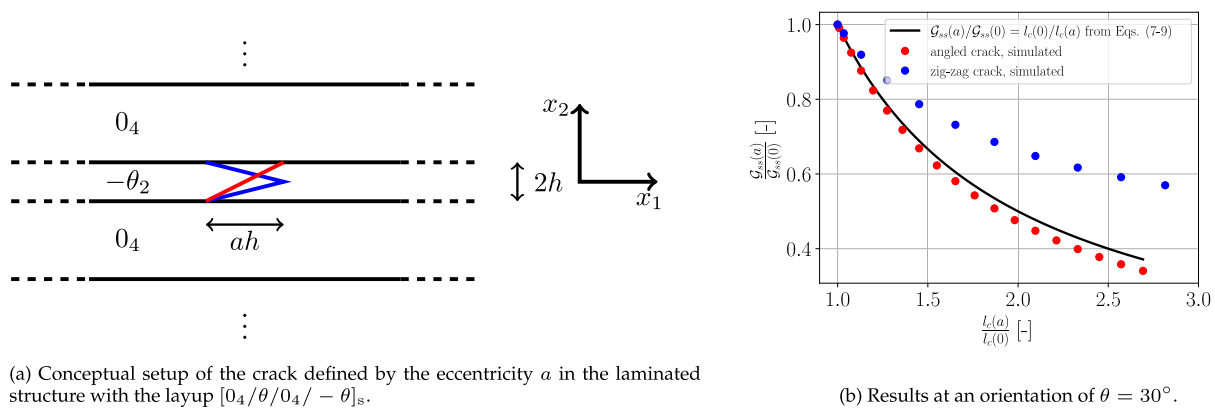


Fig. 15. Parametric study with the inclination parameter a to showcase its effect on the energy release rate G_{ss} .

inclination, $G_{ss}(a)$, can be related to the energy release rate without inclination, $G_{ss}(0)$, through

$$G_{ss}(a) = \frac{2h}{l_c} G_{ss}(0) = \frac{1}{\sqrt{1 + \frac{a^2}{4}}} G_{ss}(0). \quad (8)$$

This relation is confirmed by a simulation, taking the difference in crack opening into account in Fig. 15(b) at an orientation of $\theta = 30^\circ$. Interestingly, the energy release rate is slightly lower than the predicted curve, indicating a smaller crack opening, which is opposite to the behavior observed in the non-straight crack in Fig. 14. However, if the presented simplified case is extended with a single “zig-zag”, indicated in blue in Fig. 15(a) and with an effective crack height parametrized by the inclination a of

$$l_c(a) = 2h\sqrt{1 + a^2}, \quad (9)$$

a larger crack opening is observed. Thus both smaller and larger crack openings are possible when compared to a straight crack. The blue zig-zag crack also shows, that the change in energy release rate cannot always be attributed solely to the change of crack surface area, as large deviations occur for greater inclination values a .

Finally, a macroscopic disturbance in the realistic microstructure is considered. For this, the propagation of crack 2 is considered in the presence of neighboring cracks. Four cases are compared, the isolated crack 2, and crack 2 in combination with each of the remaining three cracks individually. Consequently, the energy release rate of crack 2 is estimated, while the other cracks are already preexisting in the model. Together with the normalized averaged crack distances between crack

2 and the other cracks $\frac{L_{crack}}{h}$, the computed energy release rates with a preexisting neighboring crack can be associated with a crack distance L_{crack} . The results are shown in Fig. 16 for $\theta = 30^\circ$ and $\theta = 60^\circ$. The non-straight cracks embedded in the microstructure are compared to straight cracks without a microstructure. While small differences are observable, the overall tendencies are similar. For smaller crack spacings L_{crack} these discrepancies do not increase between the two models, as also shown in Fig. 12 for the regular case. Thus, not only the choice of homogenization is more important than the accurate model of a fiber–matrix microstructure and non-straight crack, but also the consideration of macroscopic defects, such as neighboring cracks.

4. Conclusion

The energy release rate G_{ss} for tunneling cracks was investigated based on inhomogeneous models of a regular and realistic distribution of fibers and compared to a homogeneous case. The layup considered is $[0_4/\theta/0_4/-\theta]_s$. The homogenized material properties were obtained based on three different approaches, the Voigt–Reuss model, the Halpin–Tsai model, and a finite element-based method. Only the finite element-based method leads to results of acceptable precision. The difference between the energy release rates based on inhomogeneous and homogeneous models was found to be below 6% when using the finite element-based homogenization.

The effect of the length of the microstructure domain was investigated, and it was found, that for the given layup the microstructure domain must be seven times longer than the off-axis layer height, to obtain errors less than 1%. Additionally, the influence of neighboring

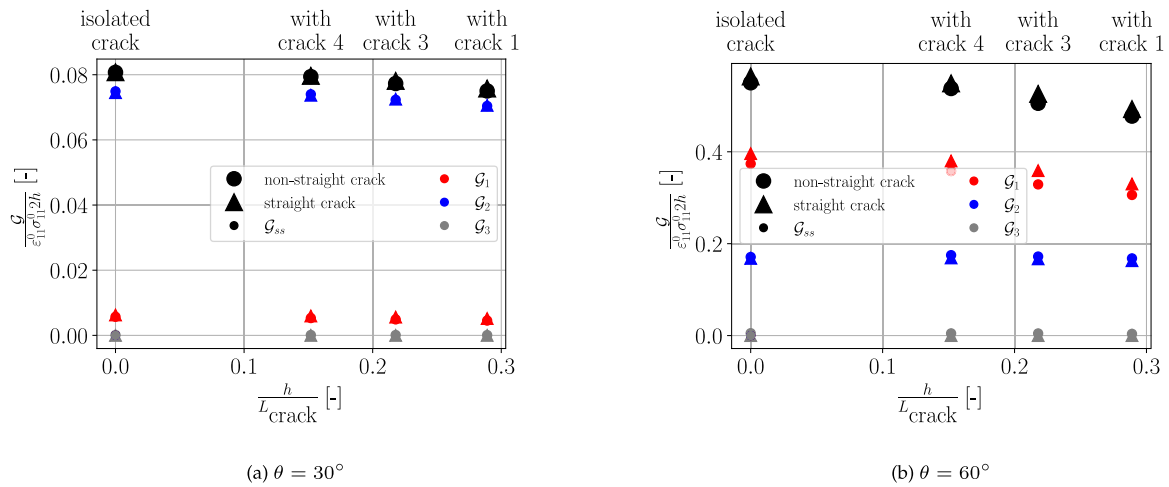


Fig. 16. Influence of the normalized distance to a preexisting neighboring crack through the spacing $\frac{h}{L_{\text{crack}}}$ on the energy release rate (of crack 2), see Fig. 6 for the location of the individual cracks.

cracks was investigated. It was shown, that the distance of the neighboring cracks has an important impact, that exceeds that of detailed modeling of the microstructure. Thus it is concluded, that the microstructure details do not have a great influence on the overall energy release rate if an accurate homogenization approach is employed.

A realistic distribution of fibers based on a scanning electron microscopy scan of a fiber–matrix microstructure was analyzed. Several complications were discussed. A highly local contact may be encountered, which was neglected in the present study. Additionally, the computation of the energy release rate via the stress extrapolation presented in [16] is not accurate enough, due to the high displacement and stress gradients, which leads to extrapolation errors. This was resolved by employing an energetically consistent approach based on nodal reaction forces and displacements. By extending the evaluation of the energy release rate to include Mode III contributions, it is possible to compute the energy release rate for arbitrary crack shapes embedded in fiber–matrix microstructures. It is shown, that approximating complex crack shapes within realistic microstructures with homogenized models and straight cracks yields accurate results, as long as an appropriate homogenization is employed. On the other hand, it is an inappropriate modeling choice to use a realistic non-straight crack in a homogenized model. Additionally, it was found that using a regular distribution of fibers as an approximation of a real fiber distribution is insufficient. Furthermore, the impact of macroscopic features, such as neighboring cracks is shown to be more important than a detailed model of the microstructure and crack shape.

CRedit authorship contribution statement

Leon Herrmann: Conceptualization, Data curation, Investigation, Writing – original draft, Writing – review & editing. **Lars P. Mikkelsen:** Conceptualization, Project administration, Writing – review & editing, Supervision. **Brian N. Legarth:** Conceptualization, Supervision, Writing – review & editing. **Christian F. Niordson:** Conceptualization, Methodology, Supervision, Writing – review & editing.

Declaration of competing interest

The authors declare that they have no known competing financial interests or personal relationships that could have appeared to influence the work reported in this paper.

Data availability

Data will be made available on request.

Appendix. Homogenization Methods

A.1. Voigt-Reuss model

The Voigt–Reuss model (see e.g. [20,26]) is an analytical method based on an iso-strain assumption for the Voigt model, also known as the rule of mixtures, and an iso-stress assumption for the Reuss model, known as the *inverse* rule of mixtures. The Voigt method is typically applied to the longitudinal Young’s modulus, E_L , and the Poisson’s ratios, ν_{LT} and $\nu_{LT'}$. The Reuss model is applied to the transverse Young’s moduli, E_T and $E_{T'}$, as well as the shear moduli, G_{LT} and $G_{LT'}$. The fiber alignment in the longitudinal direction leads to transverse isotropy, which makes the shear modulus, $G_{TT'}$, computable from the remaining parameters, such that

$$\begin{aligned} E_L &= E_f \varphi + E_m (1 - \varphi) & G_{LT} &= \frac{G_m G_f}{G_m (1 - \varphi) + G_f \varphi} & \nu_{LT} &= \nu_m (1 - \varphi) + \nu_f \varphi \\ E_T &= \frac{E_m E_f}{(1 - \varphi) E_f + \varphi E_m} & G_{LT'} &= G_{LT} & \nu_{LT'} &= \nu_{LT} \\ E_{T'} &= E_T & G_{TT'} &= \frac{E_T}{2(1 + \nu_{TT'})} & \nu_{TT'} &> \nu_m \end{aligned}$$

No analytical expression exists for the Poisson’s ratio, $\nu_{TT'}$, although it is known to be larger than ν_m , i.e. $\nu_{TT'} > \nu_m$.

A.2. Halpin–Tsai model

The Voigt–Reuss model is simple, but often not sufficiently accurate for the transverse stiffness properties. The Halpin–Tsai model [27] (or see e.g. [20]) is a semi-empirical method extending the Voigt–Reuss model, where the adjustments lie in the Reuss model for the transverse Young’s moduli, E_T , $E_{T'}$, and the shear moduli, G_{LT} , $G_{LT'}$. Thus, some of the parameters are still computed by the Voigt–Reuss model given above, but E_T , $E_{T'}$, G_{LT} and $G_{LT'}$ are instead computed as

$$\begin{aligned} E_T = E_{T'} &= E_m \frac{1 + \zeta \eta_E \varphi}{1 - \eta_E \varphi} & \eta_E &= \frac{\frac{E_f}{E_m} - 1}{\frac{E_f}{E_m} + \zeta} \\ G_{LT} = G_{LT'} &= G_m \frac{1 + \zeta \eta_G \varphi}{1 - \eta_G \varphi} & \eta_G &= \frac{\frac{G_f}{G_m} - 1}{\frac{G_f}{G_m} + \zeta} \end{aligned}$$

The shape of the fibers is taken into account via the shape parameter, which for round fibers is $\zeta = 2$. Note also, that due to the change of the transverse Young's moduli, the shear modulus $G_{TT'}$ is also modified.

A.3. Finite element based homogenization

A third alternative is a homogenization via finite element analysis using a three-dimensional model of the microstructure. Here, a model for the material system consisting of fibers and matrix is loaded for each stress component. From these simplified load cases, the homogenized constitutive matrix and the material properties can be extracted, as described in [20] for fiber-reinforced composites. The method can be used for arbitrarily complex structures such as those shown in [28]. In this work a plugin [24] for Abaqus is used, automating the homogenization process on three-dimensional models. This is shown to be the most accurate homogenization method out of the three discussed in the present paper, as it accounts for both the fiber geometry and the fiber distribution. The Abaqus plugin has been used both for the regular case sketched in Fig. 7 using a representative volume element and the realistic case using the entire fiber–matrix microstructure domain illustrated in Fig. 6.

References

- [1] Crossman F, Wang A. The dependence of transverse cracking and delamination on ply thickness in graphite/epoxy laminates. In: Reifsnider K, editor. *Damage in composite materials: basic mechanisms, accumulation, tolerance, and characterization*. ASTM International; p. 118–22. <http://dx.doi.org/10.1520/STP34324S>.
- [2] Tong J, Guild FJ, Ogin SL, Smith PA. On matrix crack growth in quasi-isotropic laminates—I. Experimental investigation. *Compos Sci Technol* 1997;57(11):1527–35. [http://dx.doi.org/10.1016/S0266-3538\(97\)00080-8](http://dx.doi.org/10.1016/S0266-3538(97)00080-8).
- [3] Raju IS, Crews JH. Interlaminar stress singularities at a straight free edge in composite laminates. *Comput Struct* 1981;14(1):21–8. [http://dx.doi.org/10.1016/0045-7949\(81\)90079-1](http://dx.doi.org/10.1016/0045-7949(81)90079-1).
- [4] Jamison R, Schulte K, Reifsnider K, Stinchcomb W. Characterization and analysis of damage mechanisms in tension-tension fatigue of graphite/epoxy laminates. In: Wilkins D, editor. *Effects of defects in composite materials*. ASTM International; p. 21–55. <http://dx.doi.org/10.1520/STP30196S>.
- [5] Jespersen KM, Mikkelsen LP. Three dimensional fatigue damage evolution in non-crimp glass fibre fabric based composites used for wind turbine blades. *Compos Sci Technol* 2017;153:261–72. <http://dx.doi.org/10.1016/j.compscitech.2017.10.004>.
- [6] Beuth JL. Cracking of thin bonded films in residual tension. *Int J Solids Struct* 1992;29(13):1657–75. [http://dx.doi.org/10.1016/0020-7683\(92\)90015-L](http://dx.doi.org/10.1016/0020-7683(92)90015-L).
- [7] Ho S, Suo Z. Tunneling cracks in constrained layers. *J Appl Mech* 1993;60(4):890–4. <http://dx.doi.org/10.1115/1.2900998>.
- [8] Ashouri Vajari D, González C, Llorca J, Legarth BN. A numerical study of the influence of microvoids in the transverse mechanical response of unidirectional composites. *Compos Sci Technol* 2014;97:46–54. <http://dx.doi.org/10.1016/j.compscitech.2014.04.004>.
- [9] Paris F, Correa E, Cañas J. Micromechanical view of failure of the matrix in fibrous composite materials. *Compos Sci Technol* 2003;63(7):1041–52. [http://dx.doi.org/10.1016/S0266-3538\(03\)00017-4](http://dx.doi.org/10.1016/S0266-3538(03)00017-4).
- [10] París F, Caño JC, Varna J. The fiber–matrix interface crack — a numerical analysis using boundary elements. *Int J Fracture* 1996;82:11–29. <http://dx.doi.org/10.1007/BF00017861>.
- [11] Cheng L, Guo T. Void interaction and coalescence in polymeric materials. *Int J Solids Struct* 2007;44(6):1787–808. <http://dx.doi.org/10.1016/j.ijsolstr.2006.08.007>.
- [12] Michel J, Moulinec H, Suquet P. Effective properties of composite materials with periodic microstructure: a computational approach. *Comput Methods Appl Mech Engrg* 1999;172(1):109–43. [http://dx.doi.org/10.1016/S0045-7825\(98\)00227-8](http://dx.doi.org/10.1016/S0045-7825(98)00227-8).
- [13] Ashouri Vajari D, Sørensen BF, Legarth BN. Effect of fiber positioning on mixed-mode fracture of interfacial debonding in composites. *Int J Solids Struct* 2015;53:58–69. <http://dx.doi.org/10.1016/j.ijsolstr.2014.10.023>.
- [14] Legarth BN, Kuroda M. Particle debonding using different yield criteria. *Eur J Mech A - Solids* 2004;23(5):737–51. <http://dx.doi.org/10.1016/j.euromechsol.2004.05.002>.
- [15] Patel DK, Waas AM. Multiscale modeling of tensile fracture in fiber reinforced composites. *Composit Part C: Open Access* 2020;2:100016. <http://dx.doi.org/10.1016/j.jcomc.2020.100016>.
- [16] Mikkelsen LP, Klitgaard SJ, Niordson CF, Sørensen BF. Tunneling cracks in arbitrary oriented off-axis lamina. *Int J Fract* 2020;226(2):161–79. <http://dx.doi.org/10.1007/s10704-020-00485-9>.
- [17] Sørensen BF, Jacobsen TK. Characterizing delamination of fibre composites by mixed mode cohesive laws. *Compos Sci Technol* 2009;69(3):445–56. <http://dx.doi.org/10.1016/j.compscitech.2008.11.025>.
- [18] Mikkelsen LP, Legarth BN, Herrmann L, Christensen MM, Niordson CF. A special finite element method applied to off-axis tunnel cracking in laminates. *Eng Fract Mech* 2022;268(April):108387. <http://dx.doi.org/10.1016/j.engfracmech.2022.108387>.
- [19] Quaresimin M, Carraro P. Damage initiation and evolution in glass/epoxy tubes subjected to combined tension–torsion fatigue loading. *Int J Fatigue* 2014;63:25–35. <http://dx.doi.org/10.1016/j.ijfatigue.2014.01.002>.
- [20] Zenkert D, Battley M. *Laminate and sandwich structures: foundations of fibre composites*. 2nd ed.. Polyteknisk Forlag; 2009.
- [21] Herrmann L, Mikkelsen LP, Legarth BN, Duddeck F, Niordson CF. An efficient stiffness degradation model for layered composites with arbitrarily oriented tunneling and delamination cracks. *Compos Sci Technol* 2022;230:109729. <http://dx.doi.org/10.1016/j.compscitech.2022.109729>.
- [22] Carraro PA, Maragoni L, Quaresimin M. Characterisation and analysis of transverse crack-induced delamination in cross-ply composite laminates under fatigue loadings. *Int J Fatigue* 2019;129:105217. <http://dx.doi.org/10.1016/j.ijfatigue.2019.105217>.
- [23] Mortensen UA, Mikkelsen LP, Andersen TL. Observations of fatigue damage in uni-directional non-crimp fabric composites subjected to cyclic bending loads. *J Compos Mater* 2022;56(23):3511–27. <http://dx.doi.org/10.1177/00219983221115795>.
- [24] McLendon R. *Micromechanics plugin for abaqus*. 2017, Simulia Learning Community.
- [25] Fosdick R, Truskinovsky L. About Clapeyron's theorem in linear elasticity. In: Man C-S, Fosdick RL, editors. *The rational spirit in modern continuum mechanics: essays and papers dedicated to the memory of clifford ambrose truesdell III*. Springer Netherlands; p. 399–426. http://dx.doi.org/10.1007/1-4020-2308-1_24.
- [26] Callister WD, Rethwisch DG. *Materials science and engineering*. 9th ed., SI version. Wiley; 2015.
- [27] Halpin JC. Effects of environmental factors on composite materials. Defense Technical Information Center; 1969. <http://dx.doi.org/10.21236/AD0692481>.
- [28] Korshunova N, Alaimo G, Hosseini S, Carraturo M, Reali A, Niiranen J, et al. Image-based numerical characterization and experimental validation of tensile behavior of octet-truss lattice structures. *Addit Manuf* 2021;41:101949. <http://dx.doi.org/10.1016/j.addma.2021.101949>.